DALTON

Density functional calculations of electronic structure, geometric structure and stability for molecular manganese sulfide clusters†

Ian G. Dance* and Keith J. Fisher

School of Chemistry, University of New South Wales, Sydney 2052, Australia

Questions about the geometrical structures, electronic structures and stabilities of $[Mn_xS_y]^-$ clusters observed in the gas phase have been approached using density functional calculations of electronic structure and energy, optimised geometrical structure, and electron affinity. Results are presented for 61 postulated isomers for 23 different compositions ranging in size from $[MnS_2]$ to $[Mn_{15}S_{15}]$, and general structural types and principles are identified. Structures based on stacks of Mn_3S_3 triangles are thermodynamically favourable, as are regular Mn_x polyhedra with (μ_3-S) caps. Structures with doubly-bridging S are frequently favourable, but there is no evidence that (μ_4-S) capping confers extra stability. Trigonal MnS_3 local co-ordination is desirable. Bonding between Mn atoms occurs throughout, at distances from *ca.* 2 Å in the smallest underco-ordinated structures up to *ca.* 2.5 Å. Electronically these clusters are characterised by a band of closely-spaced bonding molecular orbitals, composed mainly of Mn 3d atomic orbitals, at and below the Fermi level. The HOMO–LUMO gaps are generally very small, and low-lying electronic states with associated magnetic and optical properties are expected. The electron affinities generally increase with cluster size, up to *ca.* 3.5 eV.

In the preceding paper[1] we have described the formation, distribution and reactions of molecular cluster ions $[Mn_xS_y]^-$ generated by laser ablation of solid MnS. This is part of our research on the gas phase chemistry of all metal chalcogenides,[2–13] in which we have discovered that the sets of compositions (x,y) for the various metal sulfide molecular clusters $[M_xS_y]$ depend on the identity of M. The observed compositions correlate with the electron count for M, such that there is general constancy of the normalised valence electron population (the normalised sum of the metal and sulfur valence electrons[12]), largely independent of M and x. It is evident that there is a fundamental pattern of electron population, implying principles of electronic structure, affecting the compositions of stable clusters.

Inquiry into the nature of this principle raises questions about the type or types of stability, which could be thermodynamic, kinetic and/or electronic. Our experiments involve (1) synthesis of $[Mn_xS_y]^-$ by aggregation of atoms, ions and electrons in the cooling plasma formed during laser ablation of MnS(s), (2) synthesis by reaction of isolated clusters with other reagents such as H_2S, and (3) dissociation of larger clusters by energised collisions. It could be that the band of observed ions in the ion-map[1] (and the non-observance of many other compositions which might be considered reasonable according to knowledge of condensed phase chemistry) is a measure of fundamental thermodynamic stability. Alternatively, it could be that the observed ions are those which have favourable formation kinetics or are the least susceptible to further reaction. Alternatively, recognising that the measurement of anions in the gas phase involves species in competition for electrons, it could be that the observed distributions reflect the compositions with largest electron affinity.

These considerations raise another fundamental question: what are the geometrical structures of these ions? Informative spectroscopic data or diffraction data are not yet available, except for measurements of the photoelectron (PE) spectra of smaller members of the series.[14] Density functional calculations of electronic structure and energy, and of geometry by minimisation of energy, are accurate and expedient for inorganic binary molecules of this type.[15–31]

Therefore in this paper we describe our applications of density functional calculations to the questions of geometrical structure, stability and electron affinity for $[Mn_xS_y]$ clusters. Rather than examine all conceivable isomers of all observed compositions, we focus on key compositions with the objective of elucidating the principles applicable to the full series. Little is known about MnS clusters in the condensed phase, in contrast to the greater amount of information on FeS clusters,[6] and so here we are using the compositions observed in the gas phase to search for the structural principles for MnS clusters.

Density Functional Calculations

The full electronic structures and optimised geometries of postulated structures were calculated using gradient corrected (non-local) density functionals, as implemented in the program DMol.‡[,32–35] The 'blype' functionals were used, incorporating the Hartree–Fock–Slater $\rho^{\frac{1}{3}}$ local exchange function,[35] Becke's 1988 version[36] of the gradient corrected exchange functional, and the Lee–Yang–Parr[37] correlation functional which includes both local and non-local terms. The non-local corrections were applied as post-SCF perturbative corrections. The basis sets, expressed numerically rather than analytically, were generated by solution of the DF equations (for each element E) with the same functionals as used for the complete cluster. The extended basis sets employed (type DND in DMol) were double numerical, augmented with polarisation functions, and obtained by solution of the DF equations for E, E^{2+}, and with excitation of one valence electron. Core orbitals were frozen in the cluster calculations. For Mn the basis set included 1s, 2s, 2p (all frozen), 3s, 3p, 3d (×2), 4s (×2), 4p (×2); for S the basis set was 1s, 2s (both frozen), 2p, 3s (×2), 3p (×2), 3d. These DND basis sets combine efficiency and accuracy.[32] The calculations were spin restricted.

Many of the $[Mn_xS_y]$ clusters are characterised by closely spaced orbitals at the Fermi level, and consequently low-lying excited states occur. Because the objective of this investigation was to explore the broad scope of the geometry–energy hypersurfaces for many isomers, a prelude to examination of specific ground (or excited) states, the calculations of electronic struc-

† *Non-SI unit employed*: eV ≈ 1.602×10^{-19} J.

‡ DMol 96.0 , MSI, 9685 Scranton Road, San Diego, CA 92121-3752.

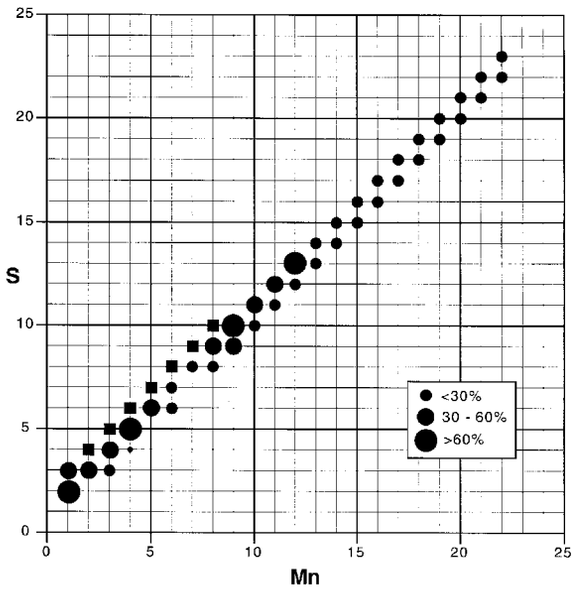

Fig. 1 Map of the compositions and abundances of the observed ions $[Mn_xS_y]^-$. The circles represent the ions formed after laser ablation of MnS, and the squares the additional products formed in reactions of $[Mn_xS_y]^-$ with H_2S

ture during geometry optimisation incorporated where necessary an averaging over close-lying states by allowing partial occupancy of orbitals close to the Fermi level. This smearing of the electron density involved orbitals within < 0.02 eV at the Fermi level, and was reduced as much as possible during the final optimisation. The energies and geometries of clusters are hardly affected (<5 kJ mol^{-1}) by smearing.

Geometry optimisation was effected by minimisation of the total energy. Second derivative calculations have not been undertaken to confirm that stationary points are energy wells, but with experience the quality of a stationary point (as minimum or saddle point) can be gleaned from the behaviour of the first derivatives during the final stages of the energy minimisations: anomalous behaviour and geometries which may not represent true minima are noted with the results. Adiabatic electron affinities have been calculated as the difference in binding energy between optimised anion and optimised neutral cluster. The optimised geometries of the neutral and anionic charge states of a cluster were very similar for all but the smallest clusters containing one or two Mn atoms. Partial charges on atoms were calculated by fitting them to the electrostatic potential (ESP) of the cluster: these ESP-derived atomic charges are generally intermediate between those calculated by the Mulliken and Hirshfeld methods.

The accuracy of the calculational method is demonstrated by the calculated electron affinity of S_3, 2.04 eV, compared with experimental measurements of 2.093 ± 0.025 [38] and 2.0 ± 0.15 eV,[39] and by the reproduction of experimental geometries for related metal chalcogenide clusters.[27,40]

Results

The compositions of the ions observed are $[Mn_xS_x]^-$ and $[Mn_xS_{x+1}]^-$ for $2 \leqslant x \leqslant 22$, excluding $[Mn_5S_5]^-$ and $[Mn_7S_7]^-$, and including $[MnS_3]^-$, together with $[Mn_xS_xO]^-$ for $4 \leqslant x \leqslant 22$, and $[Mn_xS_{x-1}O]^-$ for $x = 11$, 13, 15, 17, 18 and 22. Details of the relative abundances are provided in the preceding paper.[1] Reactions of these clusters with H_2S generate also the species $[Mn_xS_{x+2}]^-$ for $2 \leqslant x \leqslant 8$. This information about occurrence is presented pictorially in Fig. 1. Clearly there is a general stability principle that the number of chalcogenide atoms is equal to, or one or two greater than, the number of Mn atoms. In this paper the ions containing Mn and S only are investigated.

Many postulates of geometry can be made, and there are many conceivable isomers particularly for the larger clusters. The object in exploring the geometry–energy hypersurfaces is to identify the general geometrical principles which confer stability. For MnS clusters the electronic structures are such that there are usually close-lying orbitals and therefore close-lying electronic states at the Fermi level. Each state has its own surface, and complete exploration of all relevant states is a resource-expensive search for detail which is effective only *after* the broader exploration of favourable geometry, reported here. Therefore, where there are very close-lying electronic states the electronic structure is calculated effectively as an average of those states. This allows the optimisation of geometry by minimisation of energy to avoid complications of detail and to explore the geometry–energy hypersurface more efficiently.

General structural principles are evident for metal chalcogenide clusters (often with terminal heteroligands) in condensed phases.[6] However, there are very few instances of Mn clusters with sulfide,[41] selenide or telluride[42] ligands, although there is a larger number of manganese oxide clusters.[43–51] Despite this lack of manganese chalcogenide clusters, there is a close similarity between the $[Mn_xS_y]^-$ and $[Fe_xS_y]^-$ cluster distributions in the gas phase, about the line $x = y$, and there are numerous examples of clusters $[Fe_xS_yL_z]$ characterised in crystal structures.[6] Thus postulated structures for $[Mn_xS_x]$ for $x = 3$–10 follow our previous suggestions for $[Fe_xS_x]$.[5] However, the $[Mn_xS_y]^-$ series extends to higher values of x than for $[Fe_xS_y]^-$, and additional structural postulates are needed.

The fact that $x \approx y$ in the MnS clusters suggests structures which are fragments of the rock salt structure of green MnS. These fragments can also be envisaged as confacial fusions of Mn_4S_4 cubes. However, there are no marked discontinuities in ion intensity at values of x corresponding to symmetrical fragments of this lattice. For instance, the ion $[Mn_{13}S_{14}]^-$ has the composition of one unit cell of the rock–salt structure of α-MnS, but $[Mn_{13}S_{14}]^-$ is relatively weak and does not represent an intensity discontinuity in the mass spectrum. There is another structural principle for metal chalcogenide cores with the composition $[M_{3m}S_{3m}]$, namely a stacking of M_3S_3 triangles. Both of these principles are incorporated in the geometries explored below.

In the following presentation and discussion of results, the isomers for $[Mn_xS_y]$ are labelled ***x*/*y*A**, ***x*/*y*B**, *etc*. The presentation proceeds from smaller to larger clusters, accumulating understanding. Table 1 contains the calculated binding energies (BE) and electron affinities (EA) for all of the clusters calculated, together with information on the configuration of the highest occupied molecular orbital (HOMO) and the gap to the lowest unoccupied molecular orbital (LUMO). In order to compare clusters with different compositions, the binding energies of $[Mn_xS_y]$ are also tabulated per atom (*i.e.* divided by $x + y$), and symbolised as BE′. The normalised binding energies for the anions BE′(−) and the electron affinities are plotted in Figs. 2 and 3 respectively. The optimised structures are presented in the Figures, with key dimensions contained in the captions and text.§ The computational strategy regarding imposed symmetry was to optimise first in relatively high symmetry, and then to relax crucial symmetry elements in order to assess their validity in the energy-minimised structure. The idealised symmetries and the optimisation symmetries are included in Table 1.

Throughout the discussion of results the formal negative signs of BE and EA (see Table 1, Figs. 2, 3) are omitted; this is consistent with experimental measurement of −EA, as the ionisation energy of the anion.

§ All dimensions quoted are those of the anion. Bonds are drawn between Mn atoms when the distances are ⩽ 2.6 Å.

Table 1 Results of calculations on the isomers of $[Mn_xS_y]$

Isomer symbol[a] and short name	Symmetry ideal (optimum[b])	Distribution of S types	BE(0)[c]/ kJ mol^{-1}	BE(−)[d]/ kJ mol^{-1}	BE′(0)[e]/ kJ mol^{-1} atom^{-1}	BE′(−)[e]/ kJ mol^{-1} atom^{-1}	EA[f]/ eV mol^{-1}	HOMO configuration[g,h] [LUMO–HOMO gap for anion]
1/2A Linear	$D_{\infty h}$ (D_{6h})		−494	−764	−165	−255	−2.80	$(a_{1g}\ e_{2g})^4$ separated by 0.008 eV
1/2B Bent	C_{2v}		−565	−776	−188	−259	−2.19	$(a_1\ b_2)^2$ separated by 0.003 eV
1/3A Planar	D_{3h}		−976	−1295	−244	−324	−3.31	$(a_1)^2$ [0.65 eV]
1/3B (S_3)	C_{2v}		−749	−868	−232	−217	−1.23	$(b_1\ b_2)^2$ separated by 0.006 eV
2/3A Linear	$D_{\infty h}$ (D_{6h})	(μ-S)	−794	−1095	−159	−219	−3.12	$(a_{2u}\ e_{2g}\ e_{2u})^7$ separated by 0.025 eV
2/3B Mn–Mn	C_2	(μ-S)	−1148	−1407	−230	−281	−2.69	$(e)^1$ [0.37 eV]
2/3C	D_{3h}	$(\mu\text{-S})_3$	−1127	−1361	−225	−272	−2.43	$(e'')^3$ [0.59 eV]
3/3A Planar	D_{3h}	$(\mu\text{-S})_3$	−1334	−1603	−222	−267	−2.78	$(e_g)^2$ [0.065 eV]
3/4A	C_{3v}		−1843	−2088	−263	−298	−2.55	$(a_2)^2$ [0.24 eV]
3/5A	D_{3h}		−2157	−2431	−270	−304	−2.84	$(a_1'')^2$ [0.38 eV]
4/4A	D_{4h}	$(\mu\text{-S})_4$	−1725	−2041	−216	−255	−3.28	$(e_u\ b_{2u})^5$ [0.26 eV]
4/4B	D_{2d}	$(\mu\text{-S})_4$	−1940	−2253	−242	−282	−3.25	$(a_1\ e)^5$ [0.70 eV]
4/4C Cubane	T_d	$(\mu_3\text{-S})_4$	−2052	−2164	−257	−271	−1.16	$(t_1)^5$ [0.07 eV]
4/4D Stellated	D_{2d} (C_{2v})	$(\mu\text{-S})_4$	−2028	−2274	−253	−284	−2.55	$(b_2)^1$ [0.40 eV]
4/5A Stellated Mn_4 tetrahedron	C_{2v}	$(\mu\text{-S})_5$	−2526	−2788	−281	−310	−2.72	$(b_2)^1$ [0.10 eV]
4/5B Mn_4 Square	C_{4v}	$(\mu\text{-S})_4$ (μ_4-S)	−2346	−2592	−261	−288	−2.55	$(a_1)^1$ [0.37 eV]
4/5C Mn_4 Butterfly	C_{2v}	$(\mu\text{-S})_4$ (μ_4-S)	−2369	−2611	−263	−290	−2.51	$(a_1\ b_2)^1$ separated by 0.006 eV [0.14 eV]
4/6A Stellated Mn_4 tetrahedron	T_d	$(\mu\text{-S})_6$	−2925	−3209	−292	−321	−2.95	$(t_2)^5$ [0.17 eV]
4/6B Mn_4 Square	D_{4h}	$(\mu\text{-S})_4$ $(\mu_4\text{-S})_2$	−2681	−2935	−268	−293	−2.63	$(b_{1g}\ e_u)^3$ separated by 0.006 eV [0.04 eV]
5/5A	C_s	$(\mu\text{-S})_5$	−2619	−2911	−262	−291	−3.03	$(a'')^2$ [0.25 eV]
5/5B	C_s	$(\mu_3\text{-S})_3$ $(\mu\text{-S})_2$	−2738	−2958	−274	−296	−2.28	$(a'')^2$ [0.023 eV]
5/5C Intersecting square pyramids	C_{4v}	$(\mu_3\text{-S})_4$ (μ_4-S)	−2616	−2822	−262	−282	−2.14	$(b_2)^2$ [0.17 eV]
5/6A	D_{3h}	$(\mu\text{-S})_6$	−3023	−3327	−275	−302	−3.16	$(e''\ e')^4$ separated by 0.009 eV [0.26 eV]
5/6B	D_{3h}	$(\mu\text{-S})_6$	−3017	−3252	−274	−296	−2.44	$(a_1)^2$ [0.023 eV]
6/6A Stacked triangles	D_{3d}	$(\mu\text{-S})_6$	−3395	−3645	−283	−304	−2.59	$(e_g)^3$ [0.037 eV]
6/6B Fused cubes	D_{2h}	$(\mu\text{-S})_2$ $(\mu_3\text{-S})_4$	−3250	−3468	−271	−289	−2.26	$(b_{2g}\ b_{1u})^1$ separated by 0.004 eV [0.18 eV]
6/6C Stacked chairs	D_{3d}	$(\mu_3\text{-S})_6$	−3117	−3310	−260	−276	−2.01	$(a_{2u})^1$ [0.030 eV]
6/6D Basket	C_{2v}	(μ_4-S) $(\mu_3\text{-S})_4$ (μ-S)	−3389	−3599	−282	−300	−2.18	$(b_2\ a_1)^1$ separated by 0.003 eV [0.042 eV]
6/7A Monocapped stacked triangles	C_{3v}	$(\mu_3\text{-S})_7$	−3845	−4124	−296	−317	−2.89	$(e)^3$ [0.13 eV]
6/8A Bicapped stacked triangles	O_h	$(\mu_3\text{-S})_8$	−4328	−4629	−309	−331	−3.12	$(e_g)^3$ [0.075 eV]
8/8A	D_2	$(\mu_3\text{-S})_4$ $(\mu\text{-S})_4$	−4650	−4970	−291	−311	−3.31	$(b_2)^1$ [0.17 eV]
8/8B Mn_8 Square antiprism	D_{4d}	$(\mu_3\text{-S})_8$	−4361	−4673	−273	−292	−3.24	$(e_2)^1$ [0.26 eV]
8/8C Bridged cubanes	D_{2d}	$(\mu_4\text{-S})_4$ $(\mu_3\text{-S})_4$	−4465	−4694	−279	−293	−2.37	$(b_1\ e)^3$ separated by 0.018 eV [0.091 eV]
8/8D	D_{2d}		−4293	−4549	−268	−284	−2.65	$(e)^1$ [0.052 eV]
8/8E	C_2		−4666	−4924	−292	−308	−2.68	$(a_1)^1$ [0.033 eV]
8/9A Stacked triangles void Mn	C_s	$(\mu_3\text{-S})_7$ $(\mu\text{-S})_2$	−4949	−5248	−291	−309	−3.11	$(a'')^2$ [0.042 eV]
8/9B Mn_8 Square antiprism	C_{4v}	(μ_4-S) $(\mu_3\text{-S})_4$ $(\mu_3\text{-S})_4$	−4754	−5049	−280	−297	−3.07	$(e\ b_2)^5$ degenerate [0.07 eV]
8/9C	C_2	(μ_4-S) $(\mu_3\text{-S})_6$ $(\mu\text{-S})_2$	−4934	−5271	−290	−310	−3.50	$(b_1)^1$ [0.090 eV]
8/9D	C_s	$(\mu_3\text{-S})_5$ $(\mu\text{-S})_4$	−4929	−5252	−290	−309	−3.35	$(a'')^1$ [0.08 eV]
8/9E	C_s	(μ_4-S) $(\mu_3\text{-S})_8$	−5039	−5320	−296	−313	−2.92	$(a')^1$ [0.01 eV]
8/9F	C_s	$(\mu_3\text{-S})_7$ $(\mu\text{-S})_2$	−5056	−5370	−297	−316	−3.25	$(a')^1$ [0.023 eV]
8/9G	D_{3h}	$(\mu_3\text{-S})_6$ $(\mu\text{-S})_3$	−4984	−5255	−293	−309	−2.81	$(a_1'')^1$ [0.23 eV]
8/9H	D_{3h}	$(\mu_4\text{-S})_3$ $(\mu\text{-S})_6$	−4996	−5314	−2934	−313	−3.30	$(a_1')^1$ [0.18 eV]
8/9I	D_{3h}	$(\mu\text{-S})_9$	−4736	−6072	−279	−298	−3.49	$(e')^1$ [0.054 eV]
8/9J	D_{3h}	$(\mu_4\text{-S})_3$ $(\mu_3\text{-S})_6$	−4604	−4869	−271	−286	−2.75	$(a_1')^1$ [0.12 eV]
8/9K	C_{3v}	$(\mu_3\text{-S})_3$ $(\mu\text{-S})_6$	−5023	−5362	−295	−315	−3.52	$(e)^1$ [0.17 eV]
8/9L	C_{3v}	$(\mu_3\text{-S})_6$ $(\mu\text{-S})_3$	−4967	−5251	−292	−309	−2.94	$(e\ a_1)^3$ separated by 0.02 eV
9/9A Stacked triangles	D_{3h}	$(\mu_4\text{-S})_3$ $(\mu_3\text{-S})_6$	−5280	−5563	−293	−309	−2.93	$(a_2\ a_1)^2$ separated by 0.01 eV
9/9B	C_{4v}	(μ_4-S) $(\mu_3\text{-S})_4$ $(\mu\text{-S})_4$	−5107	−5380	−284	−299	−2.84	$(b_1)^2$ [0.08 eV]
10/10A	C_{2v} (C_2)	$(\mu_3\text{-S})_8$ $(\mu\text{-S})_2$	−5811	−6126	−291	−306	−3.26	$(a_2)^1$ [0.10 eV]
12/12A Stacked triangles	D_{3d}	$(\mu_4\text{-S})_6$ $(\mu_3\text{-S})_6$	−7218	−7501	−301	−313	−2.94	$(e_g)^3$ [0.07 eV]

Table 1 (*Continued*)

Isomer symbol[a] and short name	Symmetry ideal (optimum[b])	Distribution of S types	BE(0)[c]/ kJ mol^{-1}	BE(−)[d]/ kJ mol^{-1}	BE′(0)[e]/ kJ mol^{-1} atom^{-1}	BE′(−)[e]/ kJ mol^{-1} atom^{-1}	EA[f]/ eV mol^{-1}	HOMO configuration[g,h] [LUMO–HOMO gap for anion]
12/12B Mn_{12} Cuboctahedron	D_{3d}	$(\mu_4\text{-S})_6$ $(\mu_3\text{-S})_6$	−7023	−7363	−293	−307	−3.53	$(e_u)^3$ [0.26 eV]
12/12C Mn_{12} Icosahedron	T_h (D_{2h})	$(\mu_3\text{-S})_{12}$	−6731	−7091	−280	−295	−3.73	$(t)^1$ [0.17 eV]
12/13A Monocapped stacked triangles	C_{3v}	$(\mu_4\text{-S})_6$ $(\mu_3\text{-S})_7$	−7680	−7979	−307	−319	−3.10	$(e)^1$ [0.14 eV]
12/13B Mn_{12} Cuboctahedron	D_{3d}	$(\mu_6\text{-S})$ $(\mu_4\text{-S})_6$ $(\mu_3\text{-S})_6$	−7246	−7572	−290	−303	−3.38	$(e_g)^3$ [0.08 eV]
12/13C Mn_{12} Icosahedron	T_h (D_{2h})	$(\mu_{12}\text{-S})$	−6921	−7257	−277	−290	−3.49	$(t, t)^7$ separated by 0.001 eV
12/14A Bicapped stacked triangles	D_{3d}	$(\mu_3\text{-S})_{12}$	−8143	−8456	−313	−325	−3.25	$(e_g)^1$ [0.13 eV]
12/14B Mn_{12} Cuboctahedron	D_{4h}	$(\mu_4\text{-S})_6(\mu_3\text{-S})_5$	−7743	−8105	−298	−312	−3.75	$(t_{2u})^3$ [0.14 eV]
13/14A	O_h (D_{2h})	$(\mu_4\text{-S})_6$ $(\mu_3\text{-S})_8$	−8353	−8716	−309	−323	−3.76	$(t_{1u})^6$ [0.19 eV]
15/15A Stacked triangles	D_{3h}	$(\mu_4\text{-S})_9$ $(\mu_3\text{-S})_6$	−9112	−9423	−304	−314	−3.23	$(e'')^2$ [0.06 eV]
15/15B	C_s	$(\mu_3\text{-S})_{15}$	−8882	−9249	−296	−308	−3.81	$(a')^2$ [0.14 eV]

[a] See the Figs. for structural details. [b] The symmetry used in the optimisation is given in parentheses only when different from the ideal point group symmetry. [c] The total binding energy for the neutral cluster. [d] The total binding energy for the anionic cluster. [e] Total binding energy divided by the number of atoms in the cluster. [f] Electron affinity (adiabatic) defined as the binding energy of the optimised anion minus the binding energy of the optimised neutral species. [g] Orbital labels are those of the point group used in optimisation. [h] For the anion. Where very closely spaced orbitals are fractionally occupied (see text) the overall configuration and energy separation of the orbitals is given.

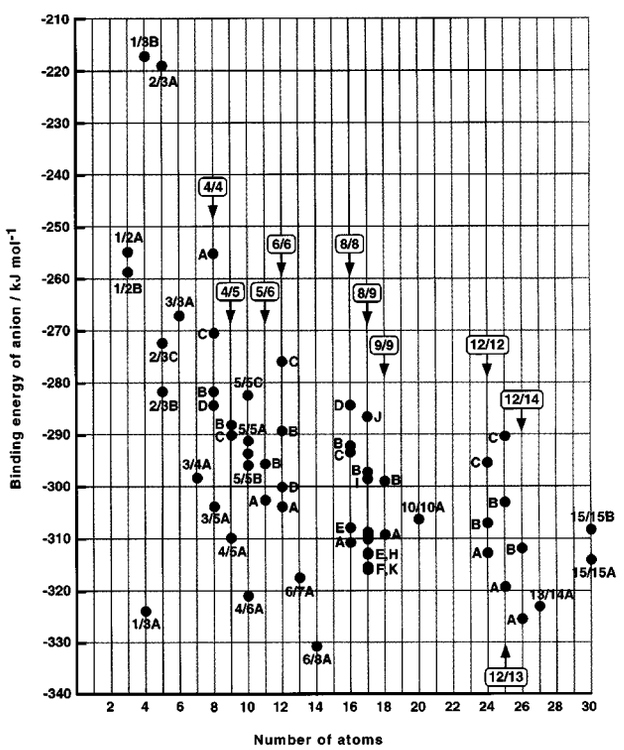

Fig. 2 The calculated normalised binding energies (kJ mol^{-1}) for isomers of the anions $[Mn_xS_y]^-$, arranged according to the numbers of atoms in the clusters ($x + y$). These are the data contained in Table 1

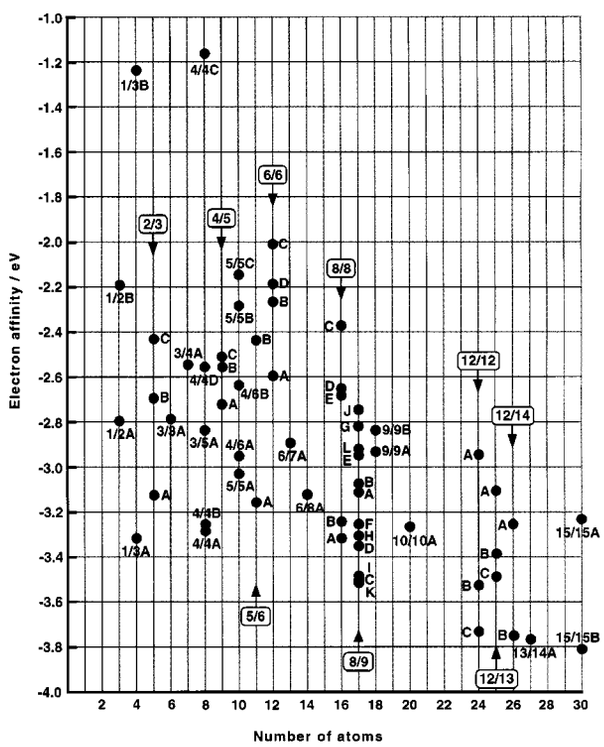

Fig. 3 The calculated electron affinities (eV) for isomers of the clusters $[Mn_xS_y]^0$, arranged according to the numbers of atoms in the clusters ($x + y$). These are the data contained in Table 1

$[MnS_2]$, $[MnS_3]$ and $[Mn_2S_3]$

These structures are shown in Fig. 4. Bent MnS_2, **1/2B**, is slightly more stable than the linear isomer **1/2A**, but the linear isomer is calculated to have a substantially larger EA. However, these small molecules are calculated to have orbitals within 0.01 eV at the Fermi level, and the geometry of **1/2B** is quite charge dependent (see Fig. 4). The isomer $Mn(\eta^2\text{-}S_2)$ was investigated and found to have a continuous surface for energy reduction down to the bent isomer **1/2B** involving insertion of Mn in the S–S bond.

Zhang *et al.*[14] measured the photoelectron spectrum of $[MnS_2]^-$ generated in a cooled pulse of helium which had passed through the plasma formed by laser vaporisation of a mixture of elemental Mn and S. Their spectrum contained both broad and sharp features with EA values of 1.32 and 2.94 eV, which they interpreted as the occurrence of two isomers: the broad feature with smaller EA was suggested to represent

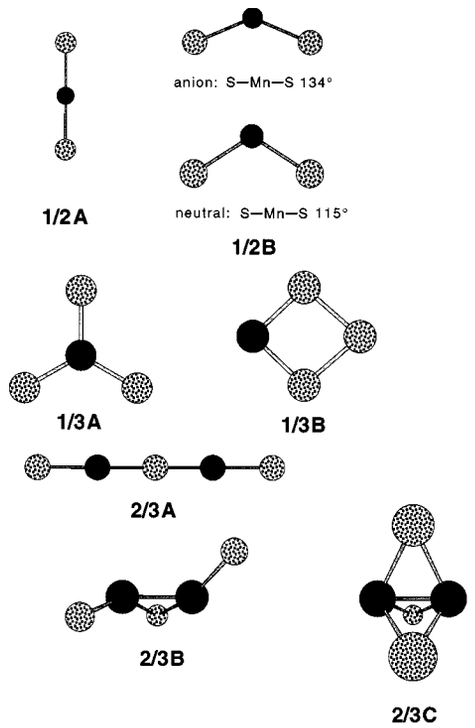

Fig. 4 The optimised structures for MnS_2, MnS_3 and Mn_2S_3. In this and all subsequent figures, dark circles are Mn, speckled circles are S

$[Mn(\eta^2\text{-}S_2)]^-$ and the sharp feature with the larger EA was attributed to the linear isomer **1/2A**. There is good agreement between the measured value of 2.94 eV and our calculation of 2.8 eV for the EA of **1/2A**. Further, we believe that the more flexible isomer **1/2B** has a smaller EA of 2.2 eV, but not as low as quoted by Zhang *et al.*, who comment that the low energy region of their spectrum is unusual.

For MnS_3, calculations of a variety of possible structures lead to the conclusion that the D_{3h} planar isomer **1/3A** is much more stable than any other geometry, including the $[Mn(S_3)]$ isomer **1/3B**. The BE′ and the EA are very favourable, and there is a 0.65 eV gap between the HOMO and LUMO in the anion. The Mn–S distance in the anion, 2.050 Å, is 0.025 Å longer than in the neutral molecule. The photoelectron spectrum for $[MnS_3]^-$ reported by Zhang *et al.*[14] shows features corresponding to an EA for $[MnS_3]$ of 1.56 eV and the onset of a feature at *ca.* 3.2 eV. Considering our calculated EA values of 1.23 eV for **1/3B** and 3.31 eV for **1/3A**, it is possible that the sample investigated by Zhang *et al.* contained both isomers.

For $[Mn_2S_3]^-$ the most stable structure is **2/3B**, which has a Mn–Mn bond (1.96 Å) with an acute μ-S bridge (Mn–S 2.23 Å), two terminal Mn–S bonds (2.07 Å), and is non-planar. Two alternative isomers are linear **2/3A**, and **2/3C** which has $(\mu_3\text{-}S)_3$ around a short (1.89 Å) Mn–Mn bond. The photoelectron spectrum[14] of $[Mn_2S_3]^-$ is ill-defined but was interpreted in terms of an EA of 1.68 eV and a suggestion of structure **2/3C**. The experimental data and our calculations are inconclusive about $[Mn_2S_3]^-$.

$[Mn_3S_3]$, $[Mn_3S_4]$ and $[Mn_3S_5]$

These three compositions are based on an Mn_3 triangle, with $(\mu\text{-}S)_3$ bridges. For Mn_3S_3 the D_{3h} isomer **3/3A** (see Fig. 5) with in-plane bridges is more stable than non-planar isomers of $Mn_3(\mu\text{-}S)_3$ in which the bridges are folded out of plane. Structure **3/3A** is a fundamental unit for many of the larger molecules: $[Mn_3S_3]^-$ has Mn–Mn 2.15 Å, Mn–S 2.24 Å, a HOMO configuration $(e_g)^2$, and a 0.065 eV separation to the LUMO. The electronic and orbital structure of **3/3A** is described below. The good agreement between the calculated EA of 2.78 eV for **3/3A** and the well defined photoelectron spectrum[14] for

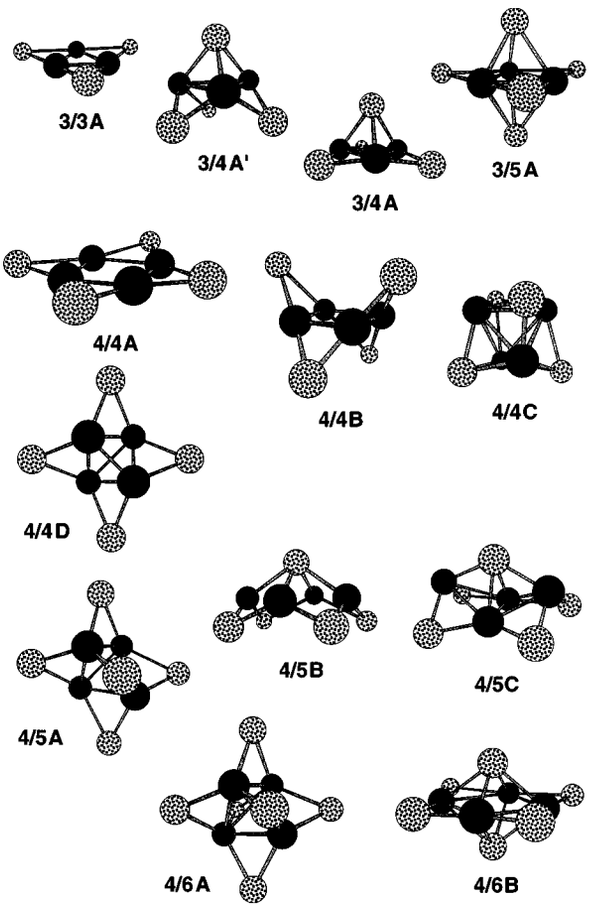

Fig. 5 Structures of the isomers of $[Mn_3S_3]$, $[Mn_3S_4]$, $[Mn_3S_5]$, $[Mn_4S_4]$, $[Mn_4S_5]$ and $[Mn_4S_6]$

$[Mn_3S_3]^-$ which shows an EA of 2.7 eV engenders confidence in the results of both investigations. On the basis of the comparative photoelectron spectra Zhang *et al.*[14] comment favourably on the **3/3A** paradigm.

For Mn_3S_4, the connectivity $Mn_3(\mu_3\text{-}S)(\mu\text{-}S)_3$ was explored. This is a fragment of the cubanoid structure M_4S_4 with one M position void, *i.e.* **3/4A′** in Fig. 5. However the optimised geometry is a modification, **3/4A**, which has the $Mn_3(\mu\text{-}S)_3$ section close to planar. This shows that the coplanarity of the $Mn_3(\mu\text{-}S)_3$ section is more influential than the symmetrical trigonal MnS_3 local co-ordination of each Mn in **3/4A′**. In **3/4A** the HOMO configuration is $(a_2)^2$ (C_{3v}), the gap to the LUMO is 0.24 eV, the Mn–(μ_3-S) distance is 2.27 Å, the Mn–(μ-S) distance is 2.22 Å, and Mn–Mn is 2.25 Å.

The optimised structure **3/5A** of Mn_3S_5 follows the pattern established in the two preceding compositions, with connectivity $Mn_3(\mu_3\text{-}S)_2(\mu\text{-}S)_3$, Mn–Mn = 2.34 Å, Mn–($\mu_3$-S) = 2.32 Å, Mn–(μ-S) = 2.22 Å. The HOMO configuration is $(a_1'')^2$ in symmetry D_{3h}, with a 0.38 eV HOMO–LUMO separation.

The BE′ and the EA both increase in the sequence **3/3A** < **3/4A** < **3/5A**. The lower values for **3/3A**, which are lower also in comparison with other nearby compositions, are consistent with the low abundance of $[Mn_3S_3]^-$ in the mass spectra: specifically the BE′ of 267 kJ mol^{-1} atom^{-1} for **3/3A** is less than 324 kJ mol^{-1} atom^{-1} for **1/3A**, 281 kJ mol^{-1} atom^{-1} for **2/3B**, 298 kJ mol^{-1} atom^{-1} for **3/4A**. The relatively high stability (BE′ 304 kJ mol^{-1} atom^{-1}) calculated for $[Mn_3S_5]^-$ (**3/5A**) is evident experimentally only as the product of addition of H_2S to $[Mn_3S_4]^-$, not through occurrence in the original laser ablation products.

$[Mn_4S_4]$

Four isomers (Fig. 5) have been explored, namely (1) **4/4A** with $Mn_4(\mu\text{-}S)_4$ connectivity in symmetry D_{4h}, (2) **4/4B** with the same

connectivity but with out-of-plane bridges and without square planarity imposed on the Mn_4 quadrilateral, (3) the well-known cubanoid $Mn_4(\mu_3\text{-}S)_4$ structure, **4/4C**, which is a face-capped Mn_4 tetrahedron, and (4) **4/4D** which is an Mn_4 tetrahedron with four edge bridges, $Mn_4(\mu\text{-}S)_4$, and stellated topology. Isomer **4/4B** optimised to square planar Mn_4 and symmetry D_{2d}; isomer **4/4C** optimised from low symmetry to T_d (although the geometry–energy surface is rather flat to deviations from T_d symmetry); and isomer **4/4D** optimised to D_{2d} in which the bridged Mn–Mn edges are 2.30 Å and the unbridged edges 2.14 Å. Isomer **4/4A** is not a transition state for interconversion of non-planar isomers like **4/4B**. The cubanoid isomer **4/4C** is not the most stable as monoanion, but is calculated to be the most stable as neutral, and accordingly it is calculated to have an unusually low EA of 1.16 eV. Isomers **4/4B** and **4/4D** have the better BE′ values as monoanions, while isomers **4/4A** and **4/4B** have competitive electron affinities.

The three isomers **4/4A**, **4/4B** and **4/4C** have closely spaced orbitals at the Fermi level: for the **4/4B** isomer of $[Mn_4S_4]^-$ an a_1 orbital and an e orbital are the highest occupied, separated by only 0.005 eV, and contain five electrons, above which there is a gap of 0.69 eV to the LUMO. However isomer **4/4D** has a HOMO–LUMO gap of 0.40 eV in the monoanion. In **4/4B** the Mn–Mn distance is 2.09 Å, and Mn–S 2.23 Å, while in **4/4D** the bridged and unbridged Mn–Mn distances are 2.30 and 2.14 Å respectively and all Mn–S distances are 2.21 Å.

The overall results (Table 1) suggest that **4/4B** is more likely to occur for $[Mn_4S_4]^-$, but are not conclusive. Detailed evaluation of the electronic states will be required in order to be more definitive about the structure of $[Mn_4S_4]^-$. However we note that $[Mn_4S_4]^-$ has very low (2%) relative intensity, and that the BE′ values for other nearby observed ions, $[Mn_3S_4]^-$ and $[Mn_4S_5]^-$, are calculated to be larger than for all isomers of $[Mn_4S_4]^-$, consistent with the relative abundances observed.

Comparison of our results with the mass spectrum and photoelectron spectrum of $[Mn_4S_4]^-$ by Zhang *et al.*[14] shows a difference in relative abundance of this ion,[1] as well as an EA of 1.53 eV which is not reproduced by the calculations. We note however that the published PE spectrum shows a feature at *ca.* 2.5 eV which could be interpreted as due to our most stable isomer **4/4D**.

$[Mn_4S_5]$ and $[Mn_4S_6]$

Three isomers (Fig. 5) have been investigated for Mn_4S_5, encompassing two connectivity types, $Mn_4(\mu\text{-}S)_5$ and $Mn_4(\mu_4\text{-}S)(\mu\text{-}S)_4$. Isomer **4/5A**, an Mn_4 tetrahedron with five edges doubly bridged, and stellated like **4/4D**, has the best BE′ and EA. For anionic **4/5A** the configuration is $(b_2)^1$ (symmetry C_{2v}) with a gap of only 0.10 eV to the LUMO: the bridged Mn–Mn distances are 2.35 and 2.41 Å, unbridged Mn–Mn is 2.03 Å, and the Mn–S distances are 2.20, 2.22 Å. Of the two $Mn_4(\mu_4\text{-}S)(\mu\text{-}S)_4$ structures, **4/5B** has symmetry C_{4v}, while **4/5C** (C_{2v}) has an additional Mn–Mn bond and the Mn_4 frame is folded in a butterfly shape: anionic **4/5C** has a central Mn–Mn bond of 2.01 Å, other Mn–Mn 2.44 Å, Mn–S distances 2.18–2.36 Å.

Two structures have been investigated for Mn_4S_6 (see Fig. 5). The stellated polyhedron **4/6A** is *tetrahedro*-Mn_4-*octahedro*-$(\mu\text{-}S)_6$ with high symmetry (T_d), while **4/6B** has connectivity $Mn_4(\mu_4\text{-}S)_2(\mu\text{-}S)_4$ with an Mn_4 square, symmetry D_{4h}. Isomer **4/6A** has the more favourable BE and EA, and its stability follows that of the related stellated isomer **4/5A**. The configurations for neutral and anionic **4/6A** are $(t_2)^4$ and $(t_2)^5$ respectively, with gaps of 0.11 and 0.17 eV to the LUMO.

$[Mn_5S_5]$ and $[Mn_5S_6]$

The anion $[Mn_5S_5]^-$ (Fig. 6) is distinctive in being absent from the mass spectrum, and therefore calculations have been undertaken in order to discern some reason for this. One relatively

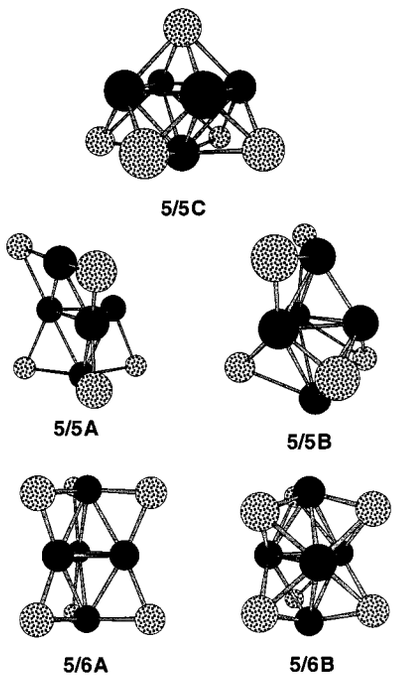

Fig. 6 Structures of the isomers of $[Mn_5S_5]$ and $[Mn_5S_6]$

symmetric (C_{4v}) structure, **5/5C**, with connectivity $Mn_5(\mu_4\text{-}S)(\mu_3\text{-}S)_4$, can be regarded as interpenetrating square pyramids of Mn_5 and S_5, but its BE′ and EA are uncompetitive. The other two isomers, **5/5A** and **5/5B** are S-void derivatives of the two Mn_5S_6 isomers **5/6A** and **5/6B** respectively. Isomers **5/6A** and **5/6B** are an informative pair, because both are D_{3h} and based on an Mn_5 trigonal bipyramid, while one (**5/6A**) has only doubly-bridging sulfide and the other (**5/6B**) has only triply-bridging sulfide. They clearly distinguish the bridging modes and the Mn^{eq} co-ordination ($Mn^{eq}S_2$ and $Mn^{eq}S_4$ respectively for **5/6A** and **5/6B**) while the Mn–Mn bonding of the core is unchanged. The $(\mu\text{-}S)_6$ isomer **5/6A** has the better BE′ and a markedly better EA, and signifies the favourability of doubly-bridging sulfide. The lesser stability of **5/6B** is probably partly due to unfavourably close approach (3.3 Å) of μ_3-S atoms. We note also that **5/6A** has more planar trigonal MnS_3 co-ordination of the two axial Mn atoms. The Mn–Mn distances also clearly reflect the differences in bridging: in both structures the $Mn^{ax}\cdots Mn^{eq}$ distance is *ca.* 2.45 Å, while the $Mn^{ax}\cdots Mn^{ax}$ distance is shorter (2.21 Å) in **5/6A** with lesser bridging than in **5/6B** (2.31 Å).

Isomers **5/5A** and **5/5B** were optimised from starting geometries obtained by removal of one S from **5/6A** and **5/6B** respectively, and in both cases the lesser co-ordinated Mn^{ax} and its two S atoms move away from the original three-fold axis. The energy differentiation of **5/6A** and **5/6B** is not retained in **5/5A** and **5/5B**, and we attribute at least part of this to the fact that **5/5B** is able to adopt more trigonal MnS_3 co-ordination and avoid the μ_3-S to μ_3-S clash of **5/6B**. However, the EA of **5/5A** exceeds that of **5/5B** by about the same margin of **5/6A** over **5/6B**.

On the basis of the BE′ and EA values a reason for our non-observation of $[Mn_5S_5]^-$ is not apparent. However we note that the mass spectrum of manganese sulfide anions generated in a different experiment contains $[Mn_5S_5]^-$ as a relatively abundant ion.[14] The PE spectrum shows onset features in the vicinity of 2 eV, in the same vicinity as our calculated EA values for **5/5B** and **5/5C**, and it could be concluded from our EA and BE calculations that isomer **5/5C** is formed in the experiments of Zhang *et al.*[14] Thus our non-observation of $[Mn_5S_5]^-$ is probably a more pronounced example of the lower general abundance of $[Mn_xS_x]^-$ ions relative to $[Mn_xS_{x+1}]^-$ and $[Mn_xS_xO]^-$ in our experiments.[1]

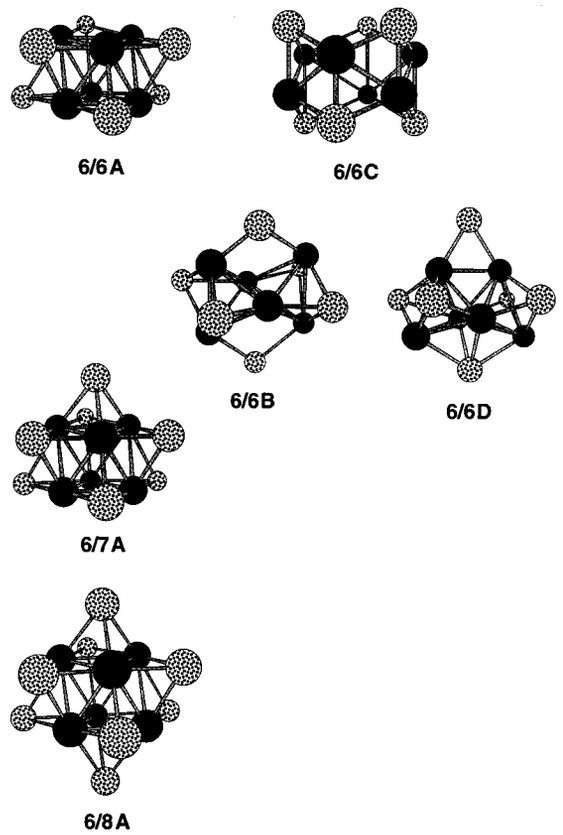

Fig. 7 Structures of the isomers of $[Mn_6S_6]$, $[Mn_6S_7]$ and $[Mn_6S_8]$

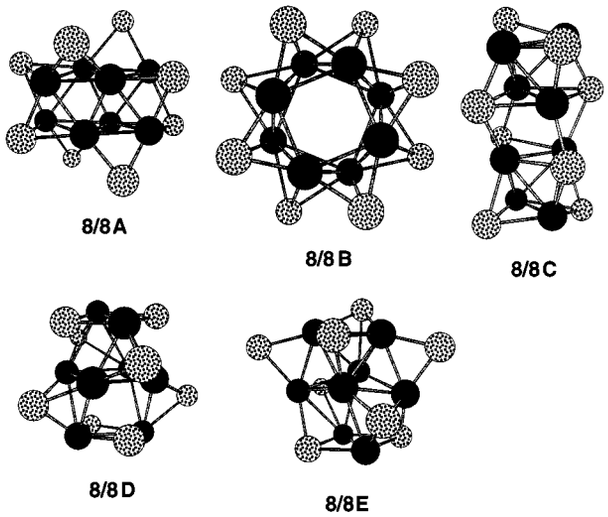

Fig. 8 Optimised structures of the five isomers for $[Mn_8S_8]^-$

$[Mn_6S_6]$

Four structure types were investigated (Fig. 7). Isomer **6/6A** is a stack of two Mn_3S_3 triangles and has the connectivity Mn_6-$(\mu_3\text{-}S)_6$, and can also be considered as an Mn_6 octahedron capped on six faces. Isomer **6/6C** has the same connectivity, but fewer Mn–Mn bonds, and can be regarded as a stack of two Mn_3S_3 cycles in chair conformation. Isomer **6/6B** was initiated as a pair of confacial cubanes, while **6/6D** is the basket structure, established in FeS cluster chemistry,[52–55] with the connectivity $Mn_6(\mu_4\text{-}S)(\mu_3\text{-}S)_4(\mu\text{-}S)$. In **6/6B** with symmetry D_{2h} the two central S atoms are geometrically unable to achieve good μ_4-S bridging: the S–Mn distances for each of these central S atoms are 2.19 Å (×2) and 2.82 Å (×2). In fact isomer **6/6D** can be regarded as an improvement of **6/6B**, in that one of the competing μ_4-S bridges in **6/6B** relaxes to a μ-S bridge in **6/6D**, allowing the other μ_4-S bridge to adopt normal geometry.

The stacked triangles isomer **6/6A** has the most favourable BE′ and EA, although the basket isomer **6/6D** has competitive BE′. The stability of **6/6A** is consistent with the stability of its half, **3/3A**. For optimised **6/6A** (symmetry D_{3d}) the HOMO configuration of the anion is $(e_g)^3$, with a very small gap of 0.04 eV to the LUMO: the Mn–Mn bond lengths are 2.35 Å within the triangles and 2.37 Å between, and the Mn–S bond lengths are 2.26 Å within the triangles and 2.40 Å between. At the Fermi level of the anion of **6/6D** there are two orbitals separated by only 0.003 eV and containing one electron.

The published PE spectrum[14] for $[Mn_6S_6]^-$ is consistent with our calculations. The first relatively weak onset occurs at *ca.* 2 eV and could be due to the occurrence of isomers **6/6C** and/or **6/6D**, while there is a more intense feature beginning at 2.6 eV which agrees very well with the calculated EA of 2.59 eV for isomer **6/6A**.

$[Mn_6S_7]$ and $[Mn_6S_8]$

Following the stability of **6/6A**, which has an octahedral Mn_6 core, the two obvious structures for Mn_6S_7 and Mn_6S_8 involve completion of the capping of the octahedron (Fig. 7). Optimised **6/7A** (symmetry C_{3v}) has in the anion the HOMO configuration $(e)^3$ with a 0.13 eV gap to the LUMO, while optimised anionic **6/8A** (symmetry O_h) has the HOMO configuration $(e_g)^3$ with a 0.07 eV gap to the LUMO. The bond lengths in **6/8A** are Mn–Mn 2.42 Å, Mn–S 2.30 Å, and those in **6/7A** are as expected intermediate between those of **6/6A** and **6/8A**, and follow the normal variations with co-ordination numbers of the bonded atoms.

The energy data (Table 1, Figs. 2 and 3) show a progressive improvement in both BE′ and EA for the sequence of related structures **6/6A**, **6/7A** and **6/8A**. It would therefore be expected that $[Mn_6S_8]^-$ would be observed in the laser ablation of MnS: however it is observed only as a product of addition of S from H_2S to $[Mn_6S_7]^-$.

At this stage it is evident from the favourable structures **3/3A**, **3/4A**, **3/5A**, **6/6A**, **6/7A** and **6/8A** that the pattern of stacked triangles, possibly with single or double caps, is a favourable structural principle. This principle leads next to the compositions 9/9 (and 9/10, 9/11), but leaves open the question of structure and structural principle for compositions which are not $x/y = 3n/3n$, $3n/3n+1$, $3n/3n+2$. Structures for Mn_8S_8 and Mn_8S_9 have been investigated to seek responses to this question.

$[Mn_8S_8]$

Five isomers of four different types have been investigated (see Fig. 8). Isomer **8/8A** is constructed as an extension of the principle of stacked triangles involving the stacking of a pair of D_{2h} Mn_4S_4 units, motif **M2**, which is an extension of the favourable D_{3h} Mn_3S_3 motif **M1**. In fact **8/8A** which has symmetry D_2 can be regarded as a stack of such units in two directions. During optimisation four of the S atoms fold away from the other unit to form μ-S rather than μ_3-S bridges. This is another indication of the favourability of μ-S bridges.

Isomer **8/8B** is a square antiprism with $(\mu_3\text{-}S)_8$. Isomer **8/8C** was constructed as a stack of three fused cubanoid Mn_4S_4 units (see **4/4C**). Isomers **8/8D** and **8/8E** can be regarded as being comprised of a central Mn_4 quadrilateral capped on opposite sides by directionally opposed Mn_2, with $(\mu_3\text{-}S)_6(\mu\text{-}S)_2$ bridging in **8/8E**. The lower stability of **8/8D** can be attributed to the poor bridging geometry of four S which although drawn as μ-S bridges could become μ_4-S except for interference with adjacent μ_3-S. The Mn_8 core of **8/8D** can also be envisaged as a fused pair of trigonal prisms.

Isomer **8/8A** is the most stable, has the best EA, and has a good HOMO–LUMO gap of 0.17 eV.

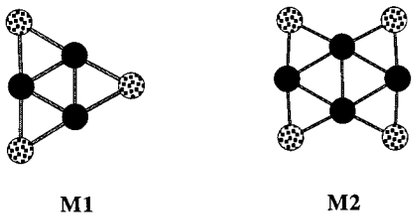

$[Mn_8S_9]$

The 12 isomers investigated have been conceived in four classes and are shown in Fig. 9. (1) Isomers in one group (**8/9A**, **8/9D**, **8/9E**, **8/9F**) have been constructed by end-addition to the **6/6A** isomer of stacked triangles, or alternatively could be considered as the triple stack of triangles, **9/9A**, without one Mn atom. This construction method was investigated with the intention of elucidating the structural principle which could generate postulates for compositions $Mn_{3n+2}S_{3n+3}$ from the favourable stacked triangle structures for $Mn_{3n}S_{3n}$. (2) In the second group isomers **8/9B** and **8/9C** have four-fold rather than three-fold conception. Isomer **8/9B** is **8/8B** with a (μ_4-S) cap. Isomer **8/9C**, which differs from **8/9B** in that it has more bonds in the tighter base, can be regarded as a staggered stack of **4/4A** on **M2**, with a (μ_4-S) cap: the bridging is (μ_4-S)(μ_3-S)$_6$(μ-S)$_2$. (3) The third group contains four isomers with a bi-triangular-capped trigonal prism of Mn_8 and different S bridges. The first isomer in this group, **8/9G**, has the same connectivity as the cluster $[Fe_7MoS_9(L^1)(L^2)(L^3)]$ (L^1 = cysteine, L^2 = homocitrate, L^3 = imidazole) at the active site of the FeMo cofactor of the enzyme nitrogenase: this cluster is significant because it provides the site for binding and facile reduction of N_2.[56–61] Each of the isomers in this group has D_{3h} symmetry, with three S atoms bridging (μ_3-S or μ-S) each of the upper and the lower Fe_4 cubanoid fragments, and three S atoms bridging (μ_4-S or μ-S) equatorially around the central Fe_6 trigonal prism. The three layers of bridging in these isomers are: **8/9G** (μ_3-S)$_3$(μ-S)$_3$(μ_3-S)$_3$; **8/9H** (μ-S)$_3$(μ_4-S)$_3$(μ-S)$_3$; **8/9I** (μ-S)$_3$(μ-S)$_3$(μ-S)$_3$; and **8/9J** (μ_3-S)$_3$(μ_4-S)$_3$(μ_3-S)$_3$. (4) The fourth set of isomers, **8/9K** and **8/9L**, are related to the previous group but have instead a *trans* bicapped octahedron as the Mn_8 core. The three layers of bridging are (μ-S)$_3$(μ_3-S)$_3$(μ-S)$_3$ in **8/9K**, and (μ-S)$_3$(μ_3-S)$_3$(μ_3-S)$_3$ in **8/9L**. A postulate with (μ-S)$_3$ around the equatorial layer of a central Mn_6 octahedron, that is structure **8/9G** with one half twisted 60° relative to the other, reverted to the trigonal prismatic central geometry of **8/9G**.

Overall, the BE′ and EA values indicate that isomer **8/9K** is the most favourable. This can be understood on the basis of the larger number of Mn–Mn bonding interactions, *together with* the occurrence of six doubly-bridging S atoms. In addition the isomers **8/9C**, **8/9D**, **8/9F** and **8/9H** are energetically competitive, and these occur in all four of the construction groups. In general the isomers with more (μ-S) linkages are more stable, and those with no such linkages (such as **8/9J**) are less favourable.

Isomers **8/9A**, **8/9D**, **8/9E** and **8/9F** ideally possess mirror symmetry, and were optimised in point group C_s. Some residual gradients in the optimised structures suggested that the true minima would have lower symmetry, but this has not been investigated.

The substantially greater stability (BE′, Table 1) of **8/9G** and **8/9H** over **8/9I** and **8/9J** can be attributed to the placement of S atoms and the local Mn co-ordination, and related to the bond lengths. All isomers have symmetry D_{3h}, and in each there are two independent Mn–Mn distances for the trigonal prism and one additional Mn–Mn distance to the polar Mn atoms; there are also two independent Mn–S distances in the cubanoid caps and one Mn–S distance for the equatorial bonds. These unique distances are presented in Fig. 9. Isomers **8/9G** and **8/9H** have approximately trigonal co-ordination, MnS_3 co-ordination at all Mn atoms, and the Mn–Mn and Mn–S bond lengths are normal and vary as expected with the connectivities of the bonded atoms. However, in **8/9I** and **8/9J** the S atoms lie in the same vertical mirror planes and consequently there is elon-

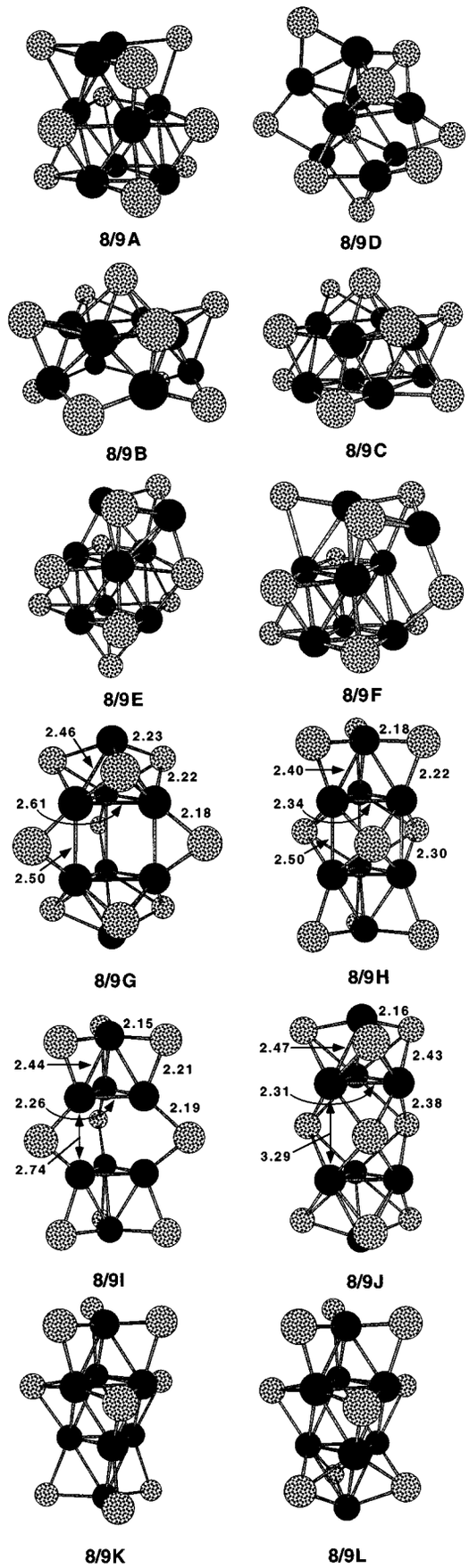

Fig. 9 The optimised structures for 12 isomers of $[Mn_8S_9]^-$. Selected interatomic distances (Å) are marked

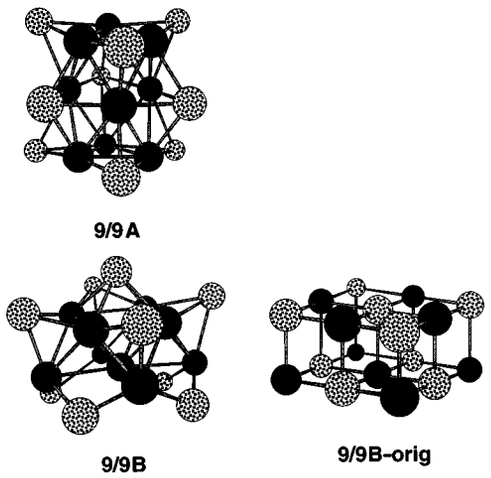

Fig. 10 The structures of the optimised isomers **9/9A** and **9/9B**, and the starting structure (**9/9B-orig**) for **9/9B**

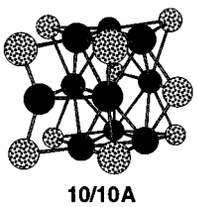

Fig. 11 The optimised structure for $[Mn_{10}S_{10}]^-$

gation of the vertical Mn–Mn distances and contraction of the horizontal Mn–Mn distances in order to relieve non-bonded repulsion between these S atoms. In **8/9J** the Mn_6 trigonal prism is strongly distorted in order to allow sufficient separation of the μ_4-S and μ_3-S atoms.

Further details of optimised M_8S_9 structures with the nitrogenase core geometry are presented separately in a paper on analogous Fe compounds.[40]

$[Mn_9S_9]$

The composition Mn_9S_9 allows two standard structure types, namely a triple stack of Mn_3S_3 triangles (isomer **9/9A**) and a $2 \times 2 \times 1$ array of cubes (isomer **9/9B**) from the close-packed lattice of solid MnS (see Fig. 10). Both change on optimisation, with appreciable change in **9/9B** such that the optimised structure bears little resemblance (other than the C_{4v} symmetry) to the starting geometry, shown as **9/9B-orig**. Optimised **9/9B** has a central Mn atom not bonded to any S atoms (and is the smallest structure with this feature), and four of the S atoms have become μ-S, allowing approximately trigonal MnS_3 co-ordination of those Mn atoms to which they are bonded.

Isomer **9/9A** is more stable and has a better EA. While the structure is ideally D_{3h}, it was found to have slightly lower energy when the three-fold symmetry was relaxed, and the optimised structure is C_{2v}. The central Mn_3 triangle in **9/9A** opens as expected owing to the greater co-ordination of these Mn atoms, and the Mn–Mn distances within the central triangle are 2.67, 2.78 (×2), in the end triangles 2.28, 2.33(x2), and 2.42, 2.43 Å between triangles.

$[Mn_{10}S_{10}]$

The one structure investigated (**10/10A**) is built from the stacked triangles **9/9A** by addition of one Mn atom in the equatorial plane: there are two μ-S bridges, and as is apparent from Fig. 11 some of the equatorial Mn–Mn connections are elongated (to 2.85 Å, not marked as bonds). The structure optimised from lower symmetry C_2 to C_{2v}. The stability and the EA of this structure are competitive with those of nearby compositions.

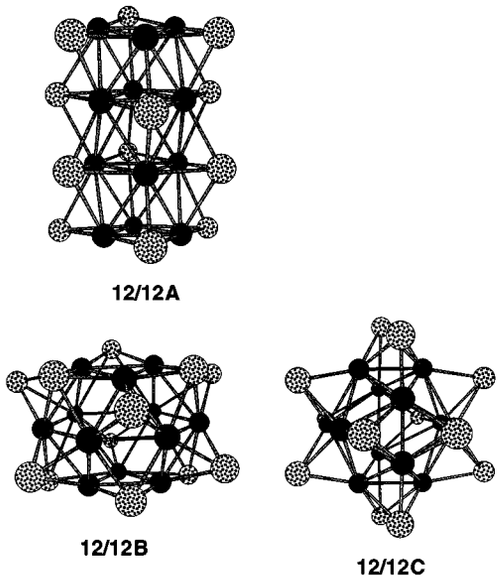

Fig. 12 The optimised structures for $[Mn_{12}S_{12}]^-$

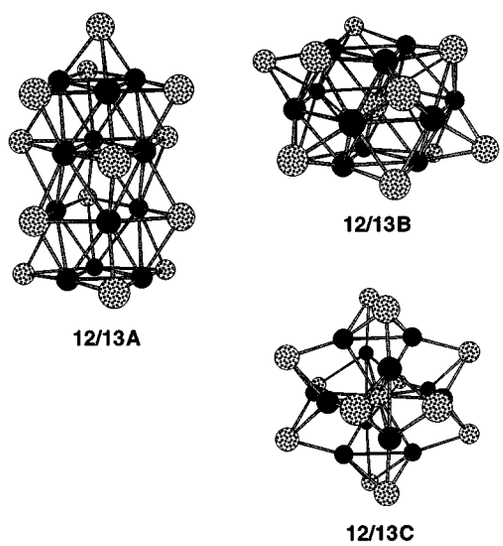

Fig. 13 The optimised structures for $[Mn_{12}S_{13}]^-$

$[Mn_{12}S_{12}]$

Three symmetrical structures with three rather different Mn_{12} frameworks were investigated (see Fig. 12). Isomer **12/12A** (D_{3d}) is a stack of four Mn_3S_3 triangles, with $(\mu_4\text{-}S)_6(\mu_3\text{-}S)_6$ bridging; **12/12B** (D_{3d}) is an Mn_{12} cuboctahedron capped $[(\mu_4\text{-}S)_6(\mu_3\text{-}S)_6]$ on all but two *trans* triangular faces; while **12/12C** (T_h) is an Mn_{12} icosahedron with $(\mu_3\text{-}S)_{12}$ capping. Alternative incomplete cappings of the Mn_{12} cuboctahedron or icosahedron were not investigated (but the fully capped cuboctahedron has been investigated, see 1**2/14C**).

The stacked triangles isomer **12/12A** is most stable. Isomer **12/12C** has the best EA (indeed close to the highest EA of all clusters investigated): there is an inverse relation between the BE values and the EA values for the three isomers of $Mn_{12}S_{12}$, which is to say that the differentiation of BE for the three isomers is greater in the neutral cluster than in the anion.

In the stacked triangles isomer **12/12A** the expansion of the central Mn_3 triangles is not as great as it was in **9/9A**: the Mn–Mn distances are 2.33 and 2.52 Å in the outer and inner layers, and 2.43 and 2.58 Å for the outer–inner and inner–inner layer connections respectively. In the icosahedron-based isomer **12/12C** the six butterfly-shaped Mn_2S_2 units which comprise it have different dimensions than the inter-Mn_2S_2 distances. Within Mn_2S_2 the distances are Mn–Mn 2.26, Mn–S 2.38 Å, while the other distances are Mn–Mn 2.45, Mn–S 2.21 Å.

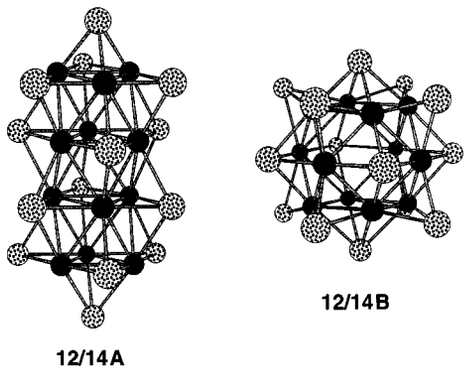

Fig. 14 The optimised structures for $[Mn_{12}S_{14}]^-$

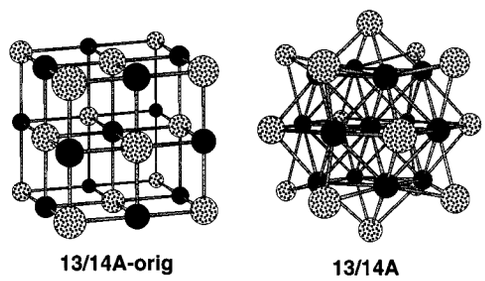

Fig. 15 The unit cell of cubic close-packed MnS (**13/14A-orig**) and the structure to which it optimises, **13/14A**, for $[Mn_{13}S_{14}]^-$

In **12/12B** there are two types of Mn, Mn^a close to the three-fold axis, and equatorial Mn^{eq}: the unique dimensions (Å) are Mn^a–Mn^a 2.36, Mn^a–Mn^{eq} 2.34, Mn^{eq}–Mn^{eq} 2.53, Mn^a–(μ_4-S) 2.29, Mn^a–(μ_3-S) 2.39, Mn^{eq}–(μ_4-S) 2.40, Mn^{eq}–(μ_3-S) 2.30.

$[Mn_{12}S_{13}]$

The ion $[Mn_{12}S_{13}]^-$ is unusually abundant in the spectrum of the products of laser ablation. Three symmetrical isomers (see Fig. 13) were constructed by addition of S to the three symmetrical $Mn_{12}S_{12}$ structures. The most stable is the isomer (**12/13A**) obtained by end-capping (μ_3-S) of the stacked triangles; the two others result from placement of S at the centre of the capped cuboctahedron, **12/13B**, or at the centre of the capped icosahedron, **12/13C**. This latter isomer contains a 12-co-ordinate central S atom (S^c), and while all of the S^c–Mn distances are equal (2.45 Å), the surface atoms aggregate slightly as six Mn_2S_2 units, as in **12/12C**. The Mn–Mn distance within the Mn_2S_2 unit is 2.52 Å, and between these units is 2.59 Å; the Mn–S distances within Mn_2S_2 are 2.34 Å and between them 2.18 Å. The expansion of **12/13C** relative to **12/12C** due to the presence of S^c occurs mainly in the Mn–Mn bond within the Mn_2S_2 aggregate, which increases from 2.26 to 2.52 Å: the Mn ··· Mn diagonals are 4.58 Å in **12/12C** and 4.90 Å in **12/13C**.

In anionic **12/13B** the six Mn^a atoms in the uncapped faces are much closer and bonded (2.27 Å) to the central S atom (S^c) than are the six equatorial Mn atoms ($S^c \cdots Mn^{eq} = 2.67$ Å). The other dimensions, following the notation used for **12/12B**, are Mn^a–Mn^a 2.47, Mn^a–Mn^{eq} 2.39, Mn^{eq}–Mn^{eq} 2.67, Mn^a–(μ_4-S) 2.31, Mn^a–(μ_3-S) 2.33, Mn^{eq}–(μ_4-S) 2.45, Mn^{eq}–(μ_3-S) 2.29 Å. The expansion of **12/12B** caused by the central S atom occurs mainly in the $(Mn^{eq})_6$ cycle.

Again there is inverse correlation of the BE and EA, although it is not as pronounced as in the isomers of $[Mn_{12}S_{12}]$.

$[Mn_{12}S_{14}]$

The two structures investigated (see Fig. 14) are symmetrical additions to previous stable structures. Isomer **12/14A** is a quadruple stack of triangles capped at each end, while **12/14B** is a totally capped cuboctahedron. Both are calculated to have high BE and high EA, and again there is an inverse correlation between these two quantities.

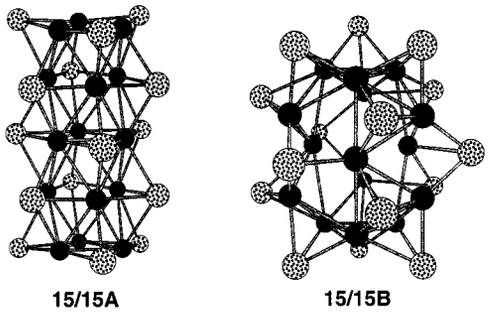

Fig. 16 The optimised structures for $[Mn_{15}S_{15}]^-$

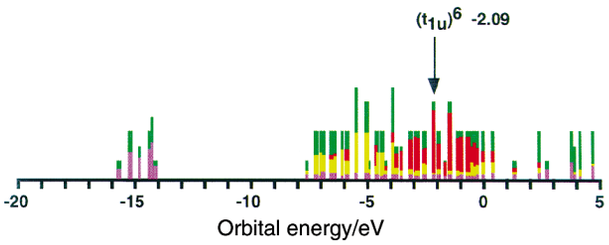

Fig. 17 Calculated energy spectrum of the molecular orbitals of **13/14A**. The lengths of the bars represent the degeneracies: the shortest bars are singlets, and the longest bars represent overlapping triplets. The highest occupied molecular orbital (HOMO) is $(t_{1u})^6$ at − 2.09 eV, almost equal in energy to two $(a_g)^2$ orbitals, and thus appears as a bar of relative length 5. The lengths (from the baseline) of the red, yellow and purple sections of the bars are the proportions of atomic orbital contributions: Mn 3d red; S 3s purple; S 3p yellow

$[Mn_{13}S_{14}]$

This is a significant composition, being that of the unit cell of cubic close-packed MnS, shown in Fig. 15 as structure **13/14A-orig**. This unit cell was optimised resulting (**13/14A**) in substantial contraction of the Mn atoms inside to form Mn–Mn bonds which are not present in the starting geometry. The symmetry of the optimised structure was O_h (lower symmetry D_{2h} was constrained during the optimisation) ; Mn–Mn bonds are all 2.48 Å, the Mn–(μ_3-S) bond length is 2.28 Å and Mn–(μ_4-S) is 2.37 Å.

We note that the BE and the EA of this structure are high, and we are unable to explain its relatively low abundance in the spectra.

$[Mn_{15}S_{15}]$

Two possible structures have been investigated and are shown in Fig. 16. Isomer **15/15A** is the standard five-fold stack of triangles with $(\mu_4\text{-S})_9(\mu_3\text{-S})_6$, while **15/15B** is based on the Frank–Kasper polyhedra,[62,63] with $(\mu_3\text{-S})_{15}$. Isomer **15/15A** is more stable, but **15/15B** has the better EA. Isomer **15/15B** has virtual three-fold symmetry (C_{3h}) but was optimised in point group C_s. Structure **15/15B**, which is relatively empty, is related to **15/15A** in that there are five three-fold layers, but the central layers in **15/15B** are more expanded. Using the labels Mn^a, Mn^t, Mn^{eq}, S^a, S^t, S^{eq} for the Mn and S atoms which are axial, tropical, and equatorial in the geographic image of this polar molecule, the key dimensions are: Mn^a–Mn^a 2.27, 2.29; Mn^a–Mn^t 2.38–2.48; Mn^t–Mn^t 4.26–4.33; Mn^{eq}–Mn^{eq} 3.05, 3.10; Mn^t–Mn^{eq} 2.54–2.63; Mn^a–Mn^{eq} 2.51–2.56; Mn^a–S^a 2.24–2.40; Mn^a–S^t 2.26–2.28; Mn^t–S^a 2.24–2.27; Mn^t–S^t 2.24–2.25; Mn^t–S^{eq} 2.21–2.22; and Mn^{eq}–S^{eq} 2.40–2.43 Å.

Electronic structures

The DF calculations provide full descriptions of the electronic structures of all isomers, information too voluminous to

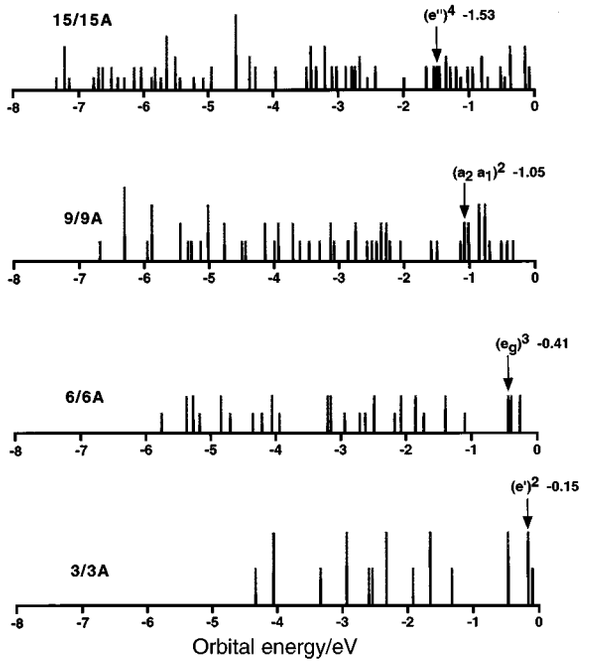

Fig. 18 Comparison of the orbital spectra of the stacked triangle isomers, **3/3A**, **6/6A**, **9/9A** and **15/15A**, showing the Mn 3d contribution as the black section of each bar. The length of the bar signifies orbital degeneracy. The HOMOs are marked

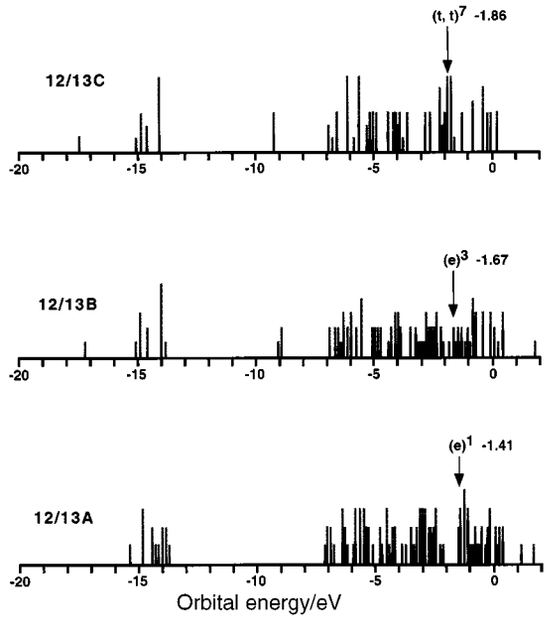

Fig. 19 Comparison of the orbital spectra of the MOs for the three isomers of $[Mn_{12}S_{13}]^-$. The length of the bar signifies orbital degeneracy, and the Mn 3d contribution is shown as the black section of each bar. The HOMOs are marked

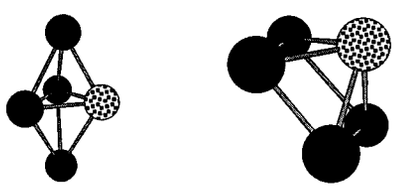

present here. Using the calculated molecular orbital energy spectra we describe the general characteristics and some specific features of the electronic structures of the anions $[Mn_xS_y]^-$.

As illustration of the general electronic structure, Fig. 17 shows the energies and compositions of the molecular orbitals of $[Mn_{13}S_{14}]^-$ **13/14A** in the region −20 to +5 eV. The set of orbitals around −15 eV are principally S 3s. There is a band of orbitals extending from −8 to 0.5 eV, and these have mainly S 3p character in the bottom section of the band and mainly Mn 3d in the top section. Most of the orbitals in this band are orbital triplets. The HOMO is $(t_{1u})^6$, at −2.09 eV, just above other filled orbitals, and there is a small gap of 0.19 eV to the LUMO. Note that the orbitals at this Fermi level are mainly Mn 3d in character.

This general orbital structure is characteristic of all of the $[Mn_xS_y]^-$ clusters. In particular, the band of closely spaced orbitals, mainly Mn 3d, either side of the Fermi level occurs in all of the larger clusters. The effect of size is illustrated in Fig. 18, which compares the orbital spectra for four of the stacked triangle isomers, **3/3A**, **6/6A**, **9/9A** and **15/15A**. Note that as the size of the stack increases the band of bonding MOs spreads and its mean energy (and the energy of the HOMO) become more negative. Note also that there are very close-lying orbitals at the HOMO.

The orbital spectrum of **6/6A** (Fig. 18) shows a substantial gap of 0.7 eV between the HOMO and next highest occupied MO (NHOMO). This property is characteristic of the related isomers **6/7A** and **6/8A** with one and two (μ_3-S) caps on the stack of triangles, for which the energy separations between the HOMO and the NHOMO are 0.7 and 0.9 eV respectively. A gap of this type is evident also in the orbital energy spectrum of **12/13A** (see Fig. 19), the monocapped stack of four triangles. However it is to be emphasised that this gap does not suggest that the oxidised forms of these isomers are significant, because in all cases there is a considerable number of electrons in the HOMO set: the HOMO configuration for each of **6/6A**, **6/7A** and **6/8A** is $(e)^3$, and for **12/13A** there are seven electrons in closely degenerate orbitals at the Fermi level.

Fig. 19 compares the orbital energy spectra for the three different isomers of $[Mn_{12}S_{13}]^-$, an abundant ion. The crowded band at the Fermi level is particularly evident in the S-centred cuboctahedral (**12/13B**) and icosahedral (**12/13C**) isomers, which also have a characteristic separate energy for the MOs with strong contributions from the central S atom, S^c: the MOs with strong S^c 3p contribution occur at −9 eV, and the S^c 3s contribution occurs at −17.5 eV.

Discussion

Geometric structural principles

Over 60 postulated structures have been investigated, and the combined results on structure and energy allow extraction of some general principles. (1) The stacked triangles motif, in **3/3A**, **6/6A**, **9/9A**, **12/12A** and **1515/A**, is more stable than any alternative construction motif postulated so far. (2) Capping of one triangular end of the stack is also a favourable geometry in the calculated structures **3/4A**, **6/7A** and **12/13A**, and it can be assumed that homologous structures would occur for Mn_9S_{10} and other members of the $[Mn_{3n}S_{3n+1}]$ series. (3) The doubly-capped stack of triangles has been calculated for **3/5A**, **6/8A** and **12/14A** and has favourable BE′ but less competitive EA. Ions $[Mn_{3n}S_{3n+2}]^-$ are not observed in the laser ablation but can be formed by addition to $[Mn_{3n}S_{3n+1}]^-$: these results suggest that EA is a factor more significant than BE′ in determining which negative ions result from the aggregation processes which follow laser ablation. (4) In the stacked-triangles structure type, the central triangles are expanded relative to the end triangles. This is related to the presence in the central triangles of (μ_4-S) bridges in a butterfly Mn_4 motif **M3**. In this motif there is conflict between favourable increase in the angular spread of the four bonds to S, and reduction in Mn–Mn bonding with increased Mn–Mn distances. The observed expansion of the central triangles (and of **M3**) is interpreted as signifying the

greater importance of the Mn–S bonding in this region. (5) The (μ_4-S)Mn_4 butterfly motif **M3** occurs also in structures **4/5C**, **6/6B**, **6/6D**, **8/9A**, **8/9C**, **8/9E** and **10/10A**. The unfavourability of **6/6B** occurs because two **M3** units are back to back and in geometrical conflict, while the favourable isomer **6/6D** has only one **M3** which adopts better geometry. (6) Motif **M4** with square (μ_4-S)Mn_4 occurs in **8/9B**, **8/9H**, **8/9J**, **9/9B**, **12/12B**, **12/13B**, **12/14B** and **13/14A**. It is not evident to us that the **M4** moiety confers stability. (7) It appears that (μ-S) bridging can be more favourable (in terms of BE) than (μ_3-S) bridging. Instances of comparison isomers, where other Mn–Mn bonding is the same and which clearly demonstrate this principle, are **4/4D** > **4/4C** and **5/6A** > **5/6B**. (8) The preceding generalisation relates to the fundamental question as to whether larger numbers of bonds (and thus higher order bridging) confer greater stability. However, it is evident that the local co-ordination stereochemistry is at least as significant as the number of bonds. Thus the occurrence of MnS_3 local co-ordination in approximately trigonal planar stereochemistry is common in many of the favourable structures: **4/6A**, **5/5B**, **6/6D**, **8/9E**, **8/9F**, **9/9B**, **12/12D**, **12/13C** and **15/15B**. A good illustration of the favourable effect of local MnS_3 co-ordination, overriding the number of bridges, is found in the BE comparisons for **8/9E**, **8/9F** > **8/9G**, **8/9H**. (9) Local MnS_4 also occurs in many of the larger structures, but often incurs S···S conflict. Structures which illustrate this point are: **5/6B**, **8/9H**, **12/12C**, **12/13C** and **13/14A**. (10) We note that the cubanoid structure Mn_4S_4 is not an important structure, in contrast to Fe_4S_4 which is a feature of iron–sulfide cluster chemistry. (11) The Mn–Mn bonding is a marked feature of all structures. This point is demonstrated clearly by the optimisation of **13/14A-orig** to **13/14A** in which each Mn atom is connected to five Mn at a distance of 2.48 Å. It is most pronounced in small structures such as **2/3C** and **4/4D** where the (μ-S) bridges provide little restraint (the acuteness of the Mn–S–Mn angle) on the Mn–Mn distances: in anionic **2/3C** the Mn–Mn distance optimises to 1.89 Å, while in **4/4D** the unbridged and bridged Mn–Mn distances are 2.14 Å and 2.21 Å respectively. As is usual in metal clusters the Mn–Mn distances depend on the co-ordination numbers of the metal atoms. (12) One of the issues for large binary clusters containing metal and a more electronegative element is whether there is segregation of the metal atoms inside (the 'core plus coating' concept) as the cluster size increases, or whether a matrix of the two types of atoms (the 'fruit cake' concept) is retained independent of size. Despite the prevalence of Mn–Mn bonding in the MnS clusters, there is no indication up to $Mn_{15}S_{15}$ that segregation is favoured. (13) Finally, we recall the caveats (*i*) that other structures not postulated or investigated here could be more stable, and (*ii*) that we have not confirmed that the optimised structures represent minima on the geometry–energy hypersurface. Nevertheless, we are confident that our results provide a valuable picture of the relevant principles of geometric structure for manganese sulfide clusters.

Electronic structural principles

(1) Close-lying orbitals occur in the vicinity of the Fermi level, and the HOMO–LUMO gaps are calculated to be in the range 0.01–0.2 eV for the majority of these structures. Low-lying electronic states are to be expected, and the electronic, optical and magnetic properties of these clusters are predicted to be very interesting. (2) The charge state of the clusters has little influence on the geometry. In the stellated isomer **4/4D** (as representative of smaller clusters) the bridged Mn–Mn distances decrease from 2.33 to 2.30 Å between neutral and anion, the unbridged Mn–Mn distance decreases from 2.18 to 2.14 Å, and the Mn–S distance increases from 2.18 to 2.21 Å; these show the Mn–Mn bonding character and slight Mn–S antibonding character of the HOMO. In the first of the stacked triangle series, **6/6A**, comparing anion with neutral: Mn–Mn intra-triangle is unchanged at 2.35 Å; Mn–Mn inter-triangle increases 2.36 to 2.37 Å; Mn–S intra-triangle increases 2.25 to 2.26 Å; and Mn–S inter-triangle increases 2.38 to 2.40 Å. By **12/12A** the differences in bond lengths between neutral and anionic clusters are less than 0.01 Å. (3) Atomic partial charges are calculated to be in the vicinity of ±0.3 for neutral clusters and $Mn^{+0.2}$, $S^{-0.4}$ for anionic clusters: as an example, in anionic **6/6D** the atomic charges are $Mn^{+\mathbf{0.25}}$, $S^{-0.42}$ in the (μ-S)Mn_2 upper section of the cluster, $Mn^{+\mathbf{0.06}}$, $S^{-0.39}$ in the central (μ_3-S)$_4$ section, and $Mn^{+\mathbf{0.36}}$, $S^{-0.42}$ in the lower (μ_4-S) section.

Photoelectron spectra

In reporting the photoelectron spectra of ions up to $[Mn_6S_6]^-$, Zhang *et al.*[14] classified the spectra as Mn_xS_2 (x = 1–4), Mn_xS_3 (x = 1–4), Mn_xS_4 (x = 2–5), Mn_xS_5 (x = 5 or 6), and Mn_6S_6, and extracted EA values from the onset of photoelectron and vertical detachment energies from the peaks. Our structural principles provide no support for these classifications on geometrical grounds. However, there is good general agreement between the experimental PE data and our density functional calculations when the possibility of structural isomers is included and the PE spectra are reconsidered as representing the overlaps of photoelectron energies from several isomers.

Related MnO clusters

Ziemann and Castleman[64] have described the formation of a collection of comparable manganese oxide clusters, all as cations, with the general formula $[Mn_xO_x]^+$ for x = 1–13, and $[Mn_xO_{x+1}]^+$ for x = 4–22. It is remarkable that the compositions of the MnS clusters and the MnO clusters (and our MnOS clusters) are virtually identical. The significance of this result is that the compositions are the same even though the formation conditions and instrumentation are different, and both anions and cations are involved. This fact alone suggests that intrinsic thermodynamic stability attends these compositions. The abundances of the $[Mn_xO_x]^+$ clusters are enhanced for x = 3, 6, 9 or 12, which is consistent with the favourability of stacked triangles structures. Ziemann and Castleman[64] proposed stacked Mn_3O_3 hexagon structures for these clusters, that is structures analogous to the stacked Mn_3S_3 triangles but without the Mn–Mn bonding. We have calculated structures for some of the MnO clusters and find that Mn–Mn bonding is important, as it is in the MnS clusters. A further point of comparison between the manganese oxide and manganese sulfide systems is that $[Mn_{13}O_{14}]^+$ and $[Mn_{13}S_{14}]^-$ both occur with low abundance. This lower stability in the gas phase (as cation or anion) of the basic unit cell of the solid further illustrates the difference between gas phase and condensed phase structures.

Thus we return to the question raised at the outset: what is the nature of the stability of the $[Mn_xS_y]^-$ clusters? From our results it would appear that the answer is thermodynamic stability, reflected in the favourable binding energies. However, we have calculated only a few of the unobserved compositions, and none well away from the pattern on the ion map, and so it is still not possible to comment on possible reasons for their non-occurrence in our experiments.

Finally, because the compositions of the $[Mn_xS_y]$ (g) clusters are similar to those of a series of $[Fe_xS_y]$ (g) clusters,[5] some transferability of the geometrical structure results from the manganese set to the iron set is expected.

Acknowledgements

The support of this research by the Australian Research Council is gratefully acknowledged.

References

1 I. G. Dance, K. J. Fisher and G. D. Willett, preceding paper.
2 J. H. El Nakat, I. G. Dance, K. J. Fisher, D. Rice and G. D. Willett, *J. Am. Chem. Soc.*, 1991, **113**, 5141.
3 J. H. El Nakat, I. G. Dance, K. J. Fisher and G. D. Willett, *Inorg. Chem.*, 1991, **30**, 2957.
4 H. J. El-Nakat, I. G. Dance, K. J. Fisher and G. D. Willett, *J. Chem. Soc., Chem. Commun.*, 1991, 746.
5 J. H. El Nakat, K. J. Fisher, I. G. Dance and G. D. Willett, *Inorg. Chem.*, 1993, **32**, 1931.
6 I. G. Dance and K. J. Fisher, *Prog. Inorg. Chem.*, 1994, **41**, 637.
7 I. G. Dance and K. J. Fisher, *Mater. Sci. Forum*, 1994, **152**, 137.
8 I. G. Dance, K. J. Fisher and G. D. Willett, *Angew. Chem., Int. Ed. Engl.*, 1995, **34**, 201.
9 I. G. Dance, K. J. Fisher and G. D. Willett, *J. Chem. Soc., Chem. Commun.*, 1995, 975.
10 I. G. Dance, K. J. Fisher and G. D. Willett, *Inorg. Chem.*, 1996, **35**, 4177.
11 K. J. Fisher, I. G. Dance and G. D. Willett, *Rapid Commun. Mass Spectrom.*, 1996, **10**, 106.
12 K. J. Fisher, I. G. Dance, G. D. Willett and M. Yi, *J. Chem. Soc., Dalton Trans.*, 1996, 709.
13 K. J. Fisher and I. G. Dance, *Polyhedron*, 1997, in the press.
14 N. Zhang, H. Kawamata, A. Nakajima and K. Kaya, *J. Chem. Phys.*, 1996, **104**, 36.
15 T. Ziegler, *Chem. Rev.*, 1991, **91**, 651.
16 T. Ziegler, *Pure Appl. Chem.*, 1991, **63**, 873.
17 A. Rosa and E. J. Baerends, *Inorg. Chem.*, 1992, **31**, 4717.
18 C. Sosa, J. W. Andzelm, B. C. Elkin, E. Wimmer, K. D. Dobbs and D. A. Dixon, *J. Phys. Chem.*, 1992, **96**, 6630.
19 T. Ziegler, *Monograph, Energetics of Organometallic Species*, ed. J.A. Martinho Simoes, Kluwer Academic Publishers, Dordrecht, 1992, pp. 357–385.
20 R. J. Deeth, *J. Chem.Soc., Faraday Trans.*, 1993, **89**, 3745.
21 R. J. Deeth, *J. Chem. Soc., Dalton Trans.*, 1993, 3711.
22 E. Folga and T. Ziegler, *J. Am. Chem. Soc.*, 1993, **115**, 5169.
23 A. Berces and T. Ziegler, *J. Phys. Chem.*, 1995, **99**, 11 417.
24 R. J. Deeth, *Struct. Bonding* (*Berlin*), 1995, **82**.
25 P. Margl, T. Ziegler and P. E. Blochl, *J. Am. Chem. Soc.*, 1995, **117**, 12 625.
26 M. R. Bray and R. J. Deeth, *Inorg. Chem.*, 1996, **35**, 5720.
27 I. G. Dance, *Transition Metal Sulfur Chemistry: Biological and Industrial Significance*, eds. E. I. Stiefel and K. Matsumoto, American Chemical Society, Washington, DC, 1996, pp. 135–152.
28 I. G. Dance, *J. Am. Chem. Soc.*, 1996, **118**, 6309.
29 I. G. Dance, *J. Am. Chem. Soc.*, 1996, **118**, 2699.
30 A. Rosa, G. Ricciardi, E. J. Baerends and D. J. Stufkens, *Inorg. Chem.*, 1996, **35**, 2886.
31 J. H. Wu and C. A. Reynolds, *J. Am. Chem. Soc.*, 1996, **118**, 10 545.
32 B. Delley, *J. Chem. Phys.*, 1990, **92**, 508.
33 B. Delley, *J. Chem. Phys.*, 1991, **94**, 7245.
34 B. Delley, *New J. Chem.*, 1992, **16**, 1103.
35 B. Delley, M. Wrinn and H. P. Lüthi, *J. Chem. Phys.*, 1994, **100**, 5785.
36 A. D. Becke, *Phys. Rev. A*, 1988, **38**, 3098.
37 C. Lee, W. Yang and R. G. Parr, *Phys. Rev. B*, 1988, **37**, 785.
38 M. R. Nimlos and G. B. Ellison, *J. Phys. Chem.*, 1986, **90**, 2574.
39 D. Feldmann, R. Rackwitz, H. J. Kaiser and E. Heinecke, *Z. Naturforsch., Teil A*, 1977, **32**, 600.
40 I. G. Dance, unpublished work.
41 H. O. Stephan, M. G. Kanatzidis and G. Henkel, *Angew. Chem., Int. Ed. Engl.*, 1996, **35**, 2135.
42 H. O. Stephan and G. Henkel, *Angew. Chem., Int. Ed. Engl.*, 1994, **33**, 2322.
43 P. D. W. Boyd, Q. Li, J. B. Vincent, K. Folting, H. R. Chang, W. E. Streib, J. C. Huffman, G. Christou and D. N. Hendrickson, *J. Am. Chem. Soc.*, 1988, **110**, 8537.
44 Q. Li, J. B. Vincent, E. Libby, H. R. Chang, J. C. Huffman, P. D. W. Boyd, G. Christou and D. N. Hendrickson, *Angew. Chem., Int. Ed. Engl.*, 1988, **27**, 1731.
45 K. S. Hagen and W. H. Armstrong, *J. Am. Chem. Soc.*, 1989, **111**, 774.
46 E. Libby, J. B. Vincent, J. C. Huffman, D. N. Hendrickson and G. Christou, *ACS Meeting Abstracts*, 1989, **197**, INOR-296.
47 A. R. Schake, J. B. Vincent, Q. Li, P. D. W. Boyd, K. Folting, J. C. Huffman, D. N. Hendrickson and G. Christou, *Inorg. Chem.*, 1989, **28**, 1915.
48 A. G. Blackman, J. C. Huffman, E. B. Lobkovsky and G. Christou, *Polyhedron*, 1992, **11**, 251.
49 A. R. Schake, H. L. Tsai, N. de Vries, R. J. Webb, K. Folting, D. N. Hendrickson and G. Christou, *J. Chem. Soc., Chem. Commun.*, 1992, 181.
50 R. Sessoli, H. L. Tsai, A. R. Schake, S. Wang, J. B. Vincent, K. Folting, D. Gatteschi, G. Christou and D. N. Hendrickson, *J. Am. Chem. Soc.*, 1993, **115**, 1804.
51 Z. Sun, P. K. Gantzel and D. N. Hendrickson, *Inorg. Chem.*, 1996, **35**, 6640.
52 M. S. Reynolds and R. H. Holm, *Inorg. Chem.*, 1988, **27**, 4494.
53 B. S. Snyder and R. H. Holm, *Inorg. Chem.*, 1988, **27**, 2339.
54 B. S. Snyder and R. H. Holm, *Inorg. Chem.*, 1990, **29**, 274.
55 B. S. Snyder, M. S. Reynolds, R. H. Holm, G. C. Papaefthymiou and R. B. Frankel, *Polyhedron*, 1991, **10**, 203.
56 B. K. Burgess, *Chem. Rev.*, 1990, **90**, 1377.
57 D. C. Rees, M. K. Chan and J. Kim, *Adv. Inorg. Chem.*, 1993, **40**, 89.
58 I. G. Dance, *Aust. J. Chem.*, 1994, **47**, 979.
59 J. Kim and D. C. Rees, *Biochemistry*, 1994, **33**, 389.
60 G. J. Leigh, *Eur. J. Biochem.*, 1995, **229**, 14.
61 I. G. Dance, *Chem. Commun.*, 1997, 165.
62 F. C. Frank and J. S. Kasper, *Acta Crystallogr.*, 1958, **11**, 184.
63 F. C. Frank and J. S. Kasper, *Acta Crystallogr.*, 1959, **12**, 483.
64 P. J. Ziemann and A. W. Castleman, *Phys. Rev. B*, 1992, **46**, 13 480.

Received 4th *February* 1997; *Paper* 7/00821J